SOFT ROBOTS

Sunlight-powered self-excited oscillators for sustainable autonomous soft robotics

Yusen Zhao[1], Qiaofeng Li[2†], Zixiao Liu[1], Yousif Alsaid[1], Pengju Shi[1], Mohammad Khalid Jawed[2], Ximin He[1,3*]

As the field of soft robotics advances, full autonomy becomes highly sought after, especially if robot motion can be powered by environmental energy. This would present a self-sustained approach in terms of both energy supply and motion control. Now, autonomous movement can be realized by leveraging out-of-equilibrium oscillatory motion of stimuli-responsive polymers under a constant light source. It would be more advantageous if environmental energy could be scavenged to power robots. However, generating oscillation becomes challenging under the limited power density of available environmental energy sources. Here, we developed fully autonomous soft robots with self-sustainability based on self-excited oscillation. Aided by modeling, we have successfully reduced the required input power density to around one-Sun level through a liquid crystal elastomer (LCE)–based bilayer structure. The autonomous motion of the low-intensity LCE/elastomer bilayer oscillator "LiLBot" under low energy supply was achieved by high photothermal conversion, low modulus, and high material responsiveness simultaneously. The LiLBot features tunable peak-to-peak amplitudes from 4 to 72 degrees and frequencies from 0.3 to 11 hertz. The oscillation approach offers a strategy for designing autonomous, untethered, and sustainable small-scale soft robots, such as a sailboat, walker, roller, and synchronized flapping wings.

INTRODUCTION

Soft robots have been pushing the boundaries of conventional robots with their intrinsic mechanical compliance and broad choices of soft materials (*1*–*3*). Using active materials, such as stimuli-responsive polymers, open up opportunities for autonomous motion and even lifelike intelligence to interact with and adapt to the environment, because environmental stimuli may be able to serve as both fuels and cues to power and regulate the soft robots. This would obviate the wired or battery power supply and even the external control by computer programming, leading to next-generation fully autonomous soft robots with self-sustainability in terms of both energy (power supply) and control (motion regulation).

It would be even more advantageous if natural, sustainable, and constant environmental sources of energy, such as mechanical vibration, sunlight, and ocean waves, could be scavenged to power the robots in a fully autonomous and self-sustainable manner to achieve sunlight-powered walking, swimming (*4*, *5*), and flapping wings. However, ambient sunlight and other sources of energy present in our natural environment are often only available at low light intensity, which imposes a challenge on continuously producing useful and practical work.

As an important means to generate locomotion, mechanical oscillation is widely observed in nature, such as in cilia axonemes, heartbeats, flapping wings, and fish undulation (*6*–*8*). These oscillations are self-regulated motions. Mimicking the intrinsic sensing-diagnosis-actuation autonomy in nature, self-excited oscillating materials based on built-in feedback loops can perform spontaneous periodic motion in response to constant external stimuli (*9*–*12*). Among them, light-driven oscillators have been realized using the self-shadowing effect of photoresponsive polymers during photoactuation and demonstrated untethered operation with omnidirectional controllability (*13*), wide operation bandwidth (1 to 270 Hz) (*12*), and great deformation programmability under broadband optical input (400 to 2500 nm) (*14*–*17*). They present potential for the design of sunlight-powered autonomous soft robots.

Among the material candidates for achieving oscillation, photoresponsive liquid crystal elastomers (LCEs) and polymer networks (LCNs) constitute a promising class of materials because of their tailorable synthesis and programmability. In terms of the actuation strategy of LCNs, the photochemical mechanism only responds to light of specific wavelengths and/or polarization and is unable to use the full spectrum of sunlight and, thus, unsuitable for practical ambient energy operation (*18*–*20*). In contrast, photothermal oscillation has the potential for sunlight application yet carries the requirement of high light input (greater than 4 Suns or 400 mW cm^{-2}). To achieve sunlight operation of oscillation, a focused lens or reflecting mirror is usually required to amplify the light intensity, making the motion generation setup more complicated (*5*, *12*).

Fundamentally, the input energy is used to photothermally heat the material, to overcome the bending stiffness, to activate the bending, and to compensate for the energy dissipation coming from damping via material viscoelasticity and air resistance. LCNs with densely cross-linked networks have high storage modulus (>100 MPa), low contraction strain (<5%), and relatively high nematic-isotropic transition temperature (T_{NI}, >60°C), demanding high energy input to reach the critical temperature and, thus, a high threshold light intensity to trigger the oscillation (*19*, *21*). Therefore, engineering both the oscillator material and structure is required for achieving high-efficiency photothermal energy transduction;

[1]Department of Material Science and Engineering, University of California Los Angeles, Los Angeles, CA 90095 USA. [2]Department of Mechanical and Aerospace Engineering, University of California Los Angeles, Los Angeles, CA 90095 USA. [3]California Nanosystems Institute, Los Angeles, CA 90095, USA.
*Corresponding author. Email: ximinhe@ucla.edu
†Present address: Massachusetts Institute of Technology, Cambridge, MA, USA.

engineering mechanical properties is needed for low bending stiffness and low viscoelasticity; and enhancing material responsiveness is required for low nematic-isotropic phase transition temperature (T_{NI}), high actuation strain, and high bending curvature.

Here, we have addressed the above challenges with a light-driven oscillator that operates under around 1-Sun level. The oscillator construct contains a candle soot (CS)–doped LCE/polydimethylsiloxane (PDMS) bilayer structure and exhibits diverse autonomous soft robotic behaviors. We named our low-intensity LCE/elastomer bilayer oscillator "LiLBot." The sunlight-powered self-oscillation was achieved through the development of high photothermal conversion, low storage modulus and loss modulus, and high material responsiveness and bending curvature. This material system successfully oscillated in the presence of the lowest light intensity of 100 mW cm^{-2} (1 Sun) and operated under natural sunlight, featuring tunable peak-to-peak amplitudes ranging from 4° to 72° (angular amplitude = 2° to 36°) and frequencies from 0.3 to 11 Hz. An oscillating working principle was established with the assistance of theoretical modeling to elucidate the physics of the complex dynamic photo–thermal-mechanical process and guided the development and optimization. This actuation motif supported various types of locomotion modes, such as walking, rolling, and propelling. We were also able to achieve collective and synchronized flapping motion of two "butterfly" wings in the presence of overhead light irradiation resembling sunlight illumination. This presented promising potential for future solar-powered microscale aerial vehicles. These findings provide insights into synthetic self-oscillating systems that could be applicable to autonomous microrobots.

RESULTS

Development and fabrication of LiLBot

In terms of the bending mechanisms of light-driven actuators, three architectures have been widely adopted, namely, multilayer (*18*), monolith with built-in gradient (*19*), and monolith with nonhomogeneous light exposure (*12*). Among them, we used a bilayered design comprising two materials with distinct deformation behavior that provides a high strain mismatch (Fig. 1A) for higher bending moment (supplementary discussion 1) and greater material and structure customizability compared with the monolithic layer designs. An elastomer-based passive layer, PDMS, can store elastic energy upon light-triggered shrinkage of the photothermally active layer, which provides an elastic restoration force for the bilayered film to unbend rapidly during the thermal-mechanical relaxation. The photothermal conversion, elastic modulus, and viscoelasticity of each individual layer can be rationally programmed and broadly tuned; this broad-range tunability is crucial for realizing oscillation under low energy input (*22*).

The oscillation was produced by a self-shadowing effect during photo–thermal-mechanical actuation and was self-regulated by the resulting built-in negative feedback loop (Fig. 1A). Upon light illumination on the LCE side, LiLBot was locally heated, and this led to bending toward the light because of strain mismatch between the LCE and the passive layer. Then, the tip bent over the incident direction of the incoming light and self-blocked the light from shining on the LiLBot. Upon shadowing, the local temperature decreased, and, subsequently, the LiLBot unbent rapidly, facilitated by the elastic recovery of the passive layer. Such a shape recovery led to light exposure again, which induced rebending, the next cycle of the oscillatory motion around the optical beam. However, as observed previously, self-shadowing might also result in static tracking of light (in-equilibrium state) (*16*) rather than a dynamic oscillation (out-of-equilibrium state) (*13*). To identify the prevailing factors in the complex light-material interaction that were involved in dynamic photo–thermal-mechanical transduction and to identify the condition that enabled the oscillation upon low input, we have developed a theoretical model. On the basis of the guiding principle discussed below, we successfully reduced the input power required to initiate oscillation close to sunlight intensity (100 mW cm^{-2}) for potential self-sustainable robots.

The actuation system is modulated by the coupling of mechanical equilibrium and thermal equilibrium. The mechanical equilibrium solely examines the thermomechanical bending capability when the LiLBot is heated, without considering the self-shadowing effect. Higher temperature T on the exposure spot leads to a higher bending angle θ. The temperature-angle (T-θ) profile is determined by the mechanical modulus, damping factor, and thermomechanical response of LCE. On the other hand, the thermal equilibrium considers how the self-shadowing affects the heating on the exposure spot at a given light intensity. At a high bending angle θ, the tip blocks the light, and equilibrium T will be reduced. The T-θ profile of thermal equilibrium is determined by the geometry, light intensity, photothermal conversion efficiency, and thermal diffusion of the LiLBot.

With the distinct T-θ profiles of the two equilibria, the dynamic system's responsive behavior tends to evolve over time. As shown in Fig. 1B, the transition from the light-tracking motion to the oscillatory motion is governed by the difference between the local derivatives of the two equilibria, as described below (see discussion S3 for detailed analysis):

$$\text{Tracking (stable)}: \beta \left.\frac{dT_m}{d\theta}\right|_{\theta=\theta_p} \geq -\left.\frac{dT_t}{d\theta}\right|_{\theta=\theta_p} \quad (1)$$

$$\text{Oscillation (unstable)}: \beta \left.\frac{dT_m}{d\theta}\right|_{\theta=\theta_p} < -\left.\frac{dT_t}{d\theta}\right|_{\theta=\theta_p} \quad (2)$$

The necessary condition for generating oscillation can be further expressed as

$$\frac{\beta k}{k_m} \leq \frac{k_p P_{in}}{k_d \theta_0} \quad (3)$$

where T_m and T_t are temperature elevations compared with environment at mechanical and thermal equilibria, respectively; θ is the instant angle; β is a system damping factor; k_p is the photothermal conversion efficiency; P_{in} is the input light power; k_d is the thermal diffusion coefficient; k_m is the moment coefficient; θ_0 is the incident light angle; and k is the stiffness of the oscillator.

From the mechanical equilibrium, smaller storage modulus (lower k), smaller loss modulus (lower β) (*23*), and a higher responsiveness to temperature change (higher k_m) favor producing oscillation. From the thermal equilibrium, higher photothermal efficiency (higher k_p) and higher light input (P_{in}) are desired for oscillation (see discussion S3 for details). Following this theoretical guide, to realize oscillation at low light intensity, we designed,

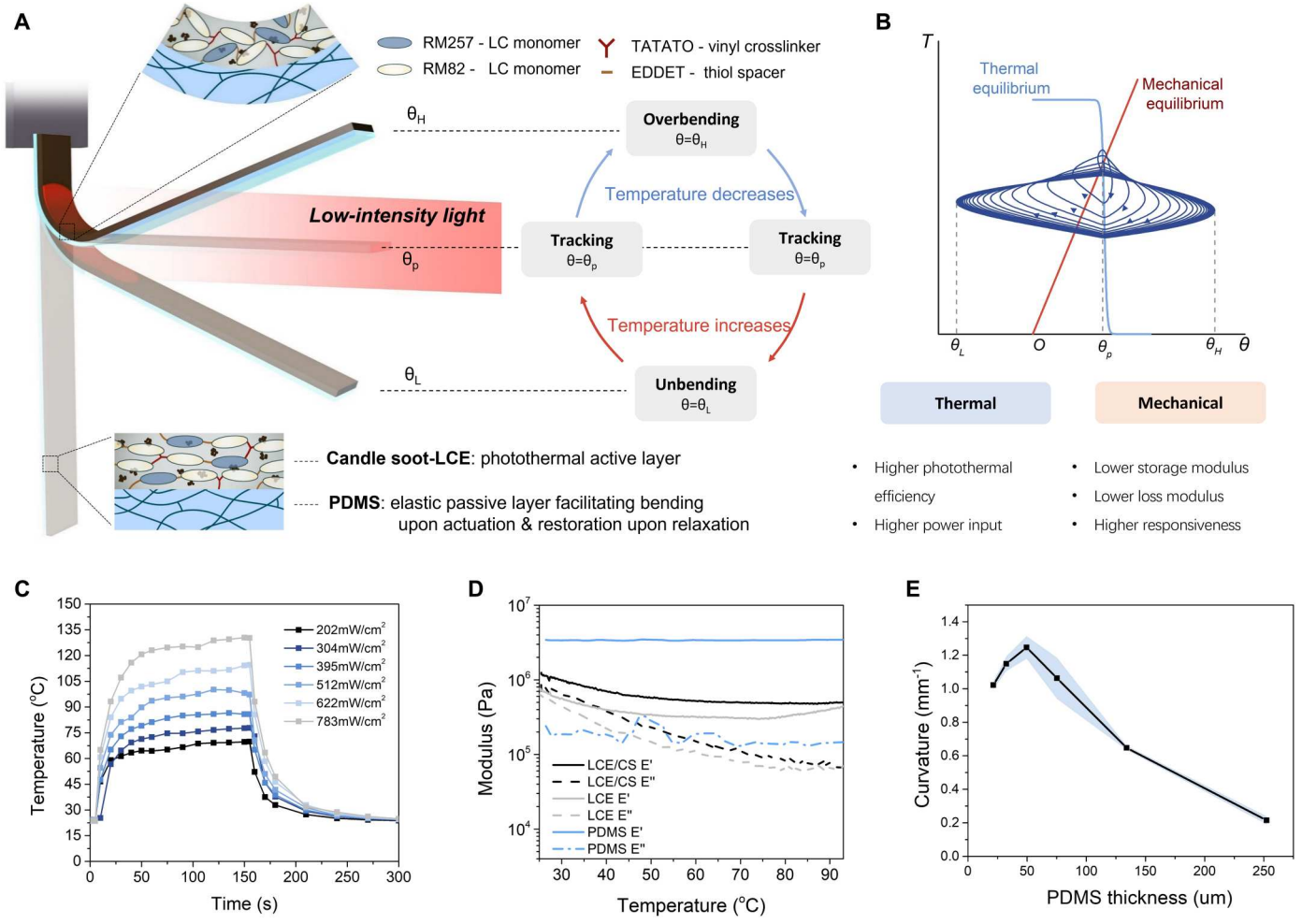

Fig. 1. Development and characterization of LiLBot. (**A**) Schematic of LiLBot flapping around the incident low-intensity optical beam, presenting an out-of-equilibrium motion. (**B**) The temperature-angle profile of the photo–thermal-mechanical system when triggered to initiate oscillation. The navy blue curve is a time-resolved plot from perturbation to steady oscillation, produced by simulation. The red curve shows the thermomechanical bending (angle θ) of LiLBot as temperature (*T*) increases, and the blue curve shows photothermal self-shadowing effect, which leads to the temperature drop at a higher bending angle. The oscillator is designed through high photothermal conversion under NIR light (**C**), reduced storage modulus and loss modulus (**D**), and improved responsiveness of LiLBot via tuning PDMS thickness (**E**). The colored shaded areas represent the SDs of the measured values (n = 3).

fabricated, and optimized the oscillating material system in the following three aspects.

Adopting high-photothermal efficiency

As a natural product from incomplete combustion of candles (paraffin wax), CS is composed of carbon nanoparticles, saturated hydrocarbons, and carboxylic compounds. It has shown high photothermal effect compared with many commonly used photoabsorbers as well as good chemical compatibility with polymers (*24*). In our previous work, we validated the high photothermal effect of CS (*25*) in the LCE composites (*26*). In this work, with the addition of 0.5 weight % (wt%) CS in a 100-μm-thick LCE film, no obvious agglomeration was observed (fig. S9), and the absorption could reach nearly 100% over visible to near-infrared (NIR) light range (400 to 1100 nm; fig. S10). Under the illumination of an 808-nm NIR laser, the surface temperature of CS-LCE film reached 70°C at 202 mW cm^{-2} and up to 130°C at 783 mW cm^{-2}, which suggested highly efficient photothermal transduction (Fig. 1C) (*27*–*29*).

Decreasing storage modulus and loss modulus

Using thiol-ene chemistry, the synthesized LCE reached a desirably low storage modulus of 1.24 MPa (Fig. 1D) owing to the existence of vinyl cross-linker, which was one to two orders of magnitude lower than the reported LCE (*30*, *31*) and three orders of magnitude lower than the reported LCN (*19*). In terms of viscoelasticity, the loss modulus of CS-LCE dropped substantially at high temperature, suggesting that the damping of the system will be reduced during actuation. Furthermore, the incorporation of PDMS as an elastic passive layer could also reduce the system damping factor β, lowering the unwanted viscous energy dissipation of the system.

Improving responsiveness with low transition temperature

The LCE made by thiol-ene chemistry was also marked by its low nematic-to-isotropic phase transition temperature (T_{NI} = 40°C;

Fig. 1E and fig. S11) (*32*), substantially lower than LCE synthesized by the thiol-acrylate reaction (>70°C) (*31*) and LCN (90°C) (*4*). The linear contraction of CS-LCE started from 30°C and reached a plateau at 60° to 70°C, with a maximum contraction ratio of 30% [$(L - L_0)/L_0$, where L and L_0 are the actuation length and original length] (fig. S12). To construct a bilayer structure with a passive layer, an LCE-oligomerized ink was printed and ultraviolet (UV) cross-linked on a PDMS film, which was prepared by spin-coating (fig. S13) and decorated by a silane coating with double bonds (fig. S8C). Such an LCE/PDMS bilayer showed good interfacial conformability (fig. S14) and adhesion (peel strength of approximately 70 N m^{-1}; fig. S15). Because of the thermal contraction mismatch of the two layers, the LCE/PDMS bilayer could bend at high temperatures. A variety of different passive layer materials (different elastomers and polymers) have been explored and tested. LiLBot with PDMS as the passive layer exhibited the highest actuation and recovery speeds, resulting in the highest amplitude oscillation under the same light intensity (table S1 and fig. S16). A thickness study showed that LiLBot with a 50-μm-thick PDMS reached the highest curvature, up to 1.24 mm^{-1} at 70°C (Fig. 1E), which was 13 times higher than LCN (0.095 mm^{-1}) at the same temperature and 4 times higher than LCE synthesized with the same chemistry with different alignment configuration (*33*). Therefore, we selected CS-LCE/PDMS bilayers for the subsequent oscillation characterization. We named the CS-LCE/PDMS bilayer as CLP bilayer and named the corresponding oscillators as LiLBotx, where "x" represented the thickness of PDMS in micrometers.

Oscillation performance of LiLBot

In the experimental setup, the LiLBot was hung vertically, and the NIR light was applied horizontally (Fig. 2A). It was observed that, as soon as the film bent toward and tracked the light, oscillation occurred within an appropriate range of input power densities named the operation window (Fig. 2B and fig. S5). Below the lower limit, the film could not oscillate or even track the light. Above the upper limit, the high light intensity caused material coiling or unstable oscillation because of the intense local photothermal effect on the tip and backside of the film as well when the film blocked the light. The middle range that corresponded to steady oscillation was the focus of this study. By varying the PDMS thickness from 21 to 250 μm (Fig. 2B), LiLBot50 was found to have the lowest threshold power of oscillation (395 mW cm^{-2}), which was in agreement with the bending curvature result (Fig. 1E). We further simulated LiLBot50 with respect to angular change over time, temperature elevation over time, amplitude in response to intensity, and threshold power of oscillation, showing good agreement with experimental results (Fig. 2C and fig. S17).

Figure 2D describes how the oscillation frequency of LiLBotx changes with the light intensity (400 to 2000 mW cm^{-2}) and the PDMS thickness (21 to 250 μm). Previous studies have found that light-driven oscillators vibrate around first-order resonant natural frequency, which is a function of the material's mechanical properties rather than light intensity (*19*). For LiLBot, the frequency increased with PDMS thickness but uncommonly decreased with light intensity. This was probably because the film naturally curled up after fabrication because of thermal stress between two layers, and thus, the distance between the tip and hinge was shortened at low light intensity, which resulted in higher natural frequency. Regarding angular amplitude, a threshold power was required to trigger the oscillation, and the peak-to-peak amplitude increased nonlinearly up to 60° (angular amplitude = 30°) with light intensity (Fig. 2E and movie S1) (*12*). Because the frequency and amplitude changed in opposite directions with increasing energy input, we used the energy density (kinetic energy divided by volume) of LiLBot to characterize the oscillation strength (Fig. 2F and discussion S2). Among oscillators with different PDMS thicknesses, LiLBot50 could generate the highest energy density (6.6 J m^{-3}) at the lowest energy input (less than 1 W cm^{-2}). The oscillating performance showed good replicability over different samples (fig. S18). On the basis of all results and analyses above, we used LiLBot50 for the subsequent experiments.

To further reduce the power of oscillation, we placed LiLBot horizontally, and the simulated solar light shone vertically on it from above (*20*, *34*). A light intensity of 100 mW cm^{-2} was sufficient to trigger chaotic oscillation, which was likely caused by environmental disturbance, such as external air currents. A light intensity greater than 110 mW cm^{-2} could trigger oscillation with consistent periodicity (Fig. 2, G to I). We have also successfully demonstrated outdoor oscillation under natural sunlight (Fig. 2, J and K). Further lowering of the required light intensity might result from the lower contribution of gravity as the restoration force, leading to more substantial bending. Ultimately, with these developments, a sunlight-powered oscillating film was successfully demonstrated, with an input power much lower than that for LCN films based on the photothermal effect (450 mW cm^{-2}) (*19*), reorientation of photoswitches (1000 mW cm^{-2}) (*12*, *15*), and other derivatives (table S2).

Robotic applications

LiLBot can be easily integrated with other materials as an actuation unit for various robotic systems. For example, we created a sunlight-powered flapping wing by assembling a nonactive polyethylene terephthalate (PET) layer as the passive wing with the CLP film exclusively as the active hinge "muscle" (fig. S19). On the basis of experiments of the PET length and NIR light power intensity, the flapping frequency and peak-to-peak amplitude could be orthogonally controlled, ranging from 3 to 11 Hz and 4° to 72°, respectively. The lowest power reached was 175 mW cm^{-2}, when PET length was 1.25 cm. Similarly, using simulated solar light as the energy source to mimic the potential outdoor application, the flapping wing could oscillate upon illumination of 240 mW cm^{-2} (fig. S20). We further characterized the performance of our design by constructing and comparing identical wings made with CLP and LCN as the oscillating muscles. Compared with the LCN wing, the CLP wing demonstrated notably higher amplitude and effectively lowered the input power required for oscillation (fig. S21). On the basis of the analysis, we used the CLP configuration for soft robotic applications with low light intensity.

Sailboat: Untethered propulsion on water

Taking advantage of the low-intensity oscillation and large-amplitude flapping of such a CLP wing configuration, we further designed a phototactic sailboat (Fig. 3A). To power the sailboat under low light intensity, we chose in-air oscillation rather than underwater actuation considering the relatively lower thermal diffusion (k_d), thermal conduction, and energy dissipation in air (*13*). A CLP wing, mounted on a plastic boat floating on water and shone on by a horizontal NIR light, provided airflow that propelled the boat forward away from the light source, exhibiting a negative

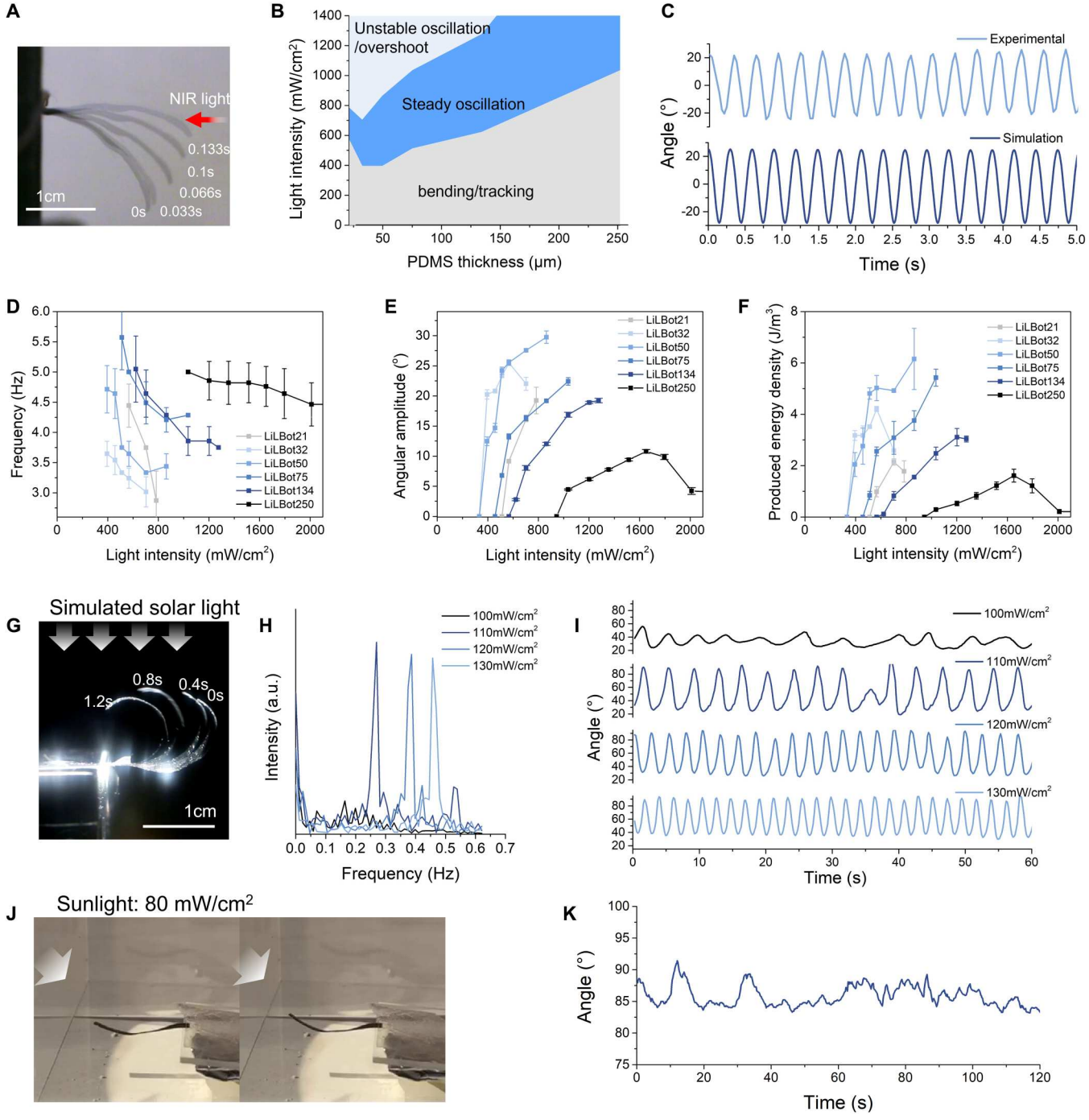

Fig. 2. Characterization of LiLBot. (**A**) Superimposed sequential snapshots of the oscillator during a half oscillation cycle using a horizontal illumination mode. (**B**) Oscillation operation window with respect to different PDMS thicknesses and light intensities. (**C**) Comparison of simulation and experimental results. PDMS thickness of 50 μm, length of 2.2 cm, and NIR light intensity of 700 mW cm^{-2}. (**D** to **F**) Frequency changes, angular amplitude changes, and produced energy densities of oscillation at different light intensities using a horizontal illumination mode. The error bars represent the SDs of the mean values obtained from five different measurements. (**G** to **I**) Superimposed sequential snapshots, angle changes, and frequencies of oscillation powered by a solar simulator using a vertical illumination mode. Light intensity in (G) is 130 mW cm^{-2}, and those in (H) and (I) range from 100 to 130 mW cm^{-2}. *Y* axis in (H) is the Fourier transform intensity of frequency. (**J** and **K**) Superimposed sequential snapshots and angle changes of oscillation powered by natural sunlight (light intensity of 80 mW cm^{-2}).

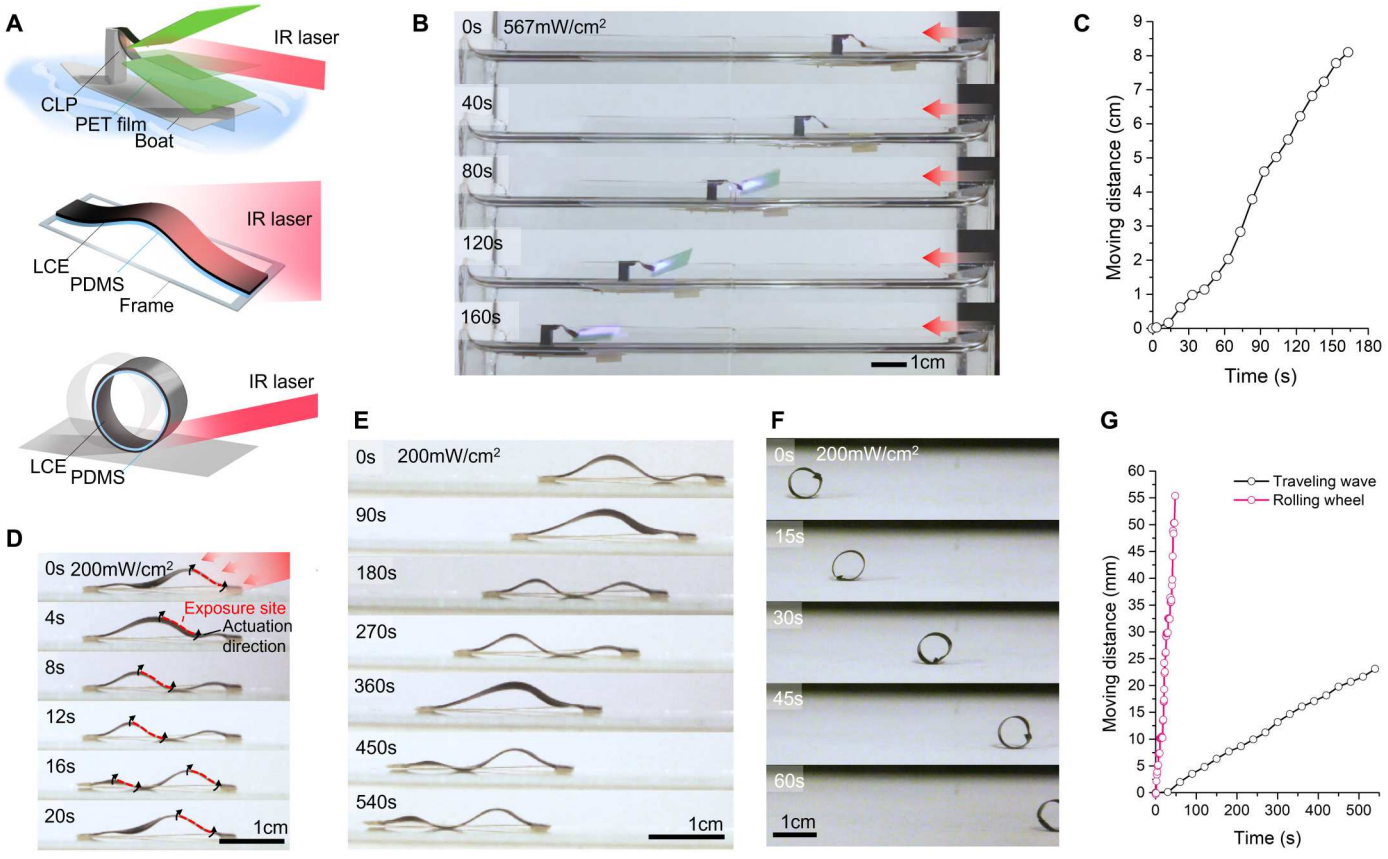

Fig. 3. Applications of the sunlight-powered LC-based oscillator in soft robots. (**A**) Schematics of CLP-based sailboat, walker, and roller under constant light. (**B**) Sequential snapshots of a sailboat under horizontal light. Light intensity was equivalent to 567 mW cm^{-2}. (**C**) Moving distance of the sailboat over time. (**D**) Sequential snapshots of a traveling wave walker in one cycle. Light intensity of 202 mW cm^{-2}. (**E**) Sequential snapshots of the walker over a period of 540 s. (**F**) Sequential snapshots of a roller over a period of 60 s. (**G**) Comparison of moving distance over time between the traveling wave walker and roller.

phototactic swimming motion. This proof-of-concept sailboat demonstrated a 31 mm min^{-1} continuous swimming speed with 567 mW cm^{-2} optical input (Fig. 3, B and C). It presented much faster directional locomotion with substantially lower energy input compared with the oscillating hydrogel-based swimmer (18 mm min^{-1} with approximately 51 kW cm^{-2}) (*13*). To further improve the speed, future investigation should focus on enhancement of the oscillation performance, increasing the number of wings, and breaking reciprocity with a time-asymmetric stroke pattern or nonreciprocal trajectory (*35*).

Walker: Directional crawling and rolling

Mimicking the traveling wave motions of earthworms, snails, and caterpillars, we demonstrated a territorial walking robot using photo-oscillation to produce directional locomotion efficiently (*36*). Under an incident NIR light at a tilt angle of 10°, the CLP film constrained using a plastic frame could perform nonreciprocal wave propagation motion because of the shadowing of the back wave and continuous regeneration of the new wave (Fig. 3D). Note that the movement does not rely on the asymmetric contact of the robot with the substrate or the surface grating (such as ratchet) as previously reported. Over a lower-intensity constant light (202 mW cm^{-2}), this walker demonstrated forward motion at a speed of 2.68 mm min^{-1} on glass (Fig. 3, E and G). This moving speed is relatively low, compared with previously reported LCN wave-propagating walkers, because of the lower modulus of the LCE yielding less stress and lower actuation frequency. Alternatively, we achieved rolling motion at the same light intensity but at much higher moving speed (72 mm min^{-1}; Fig. 4F). The continuous rolling was generated by illumination on only one side of the roller, which caused the curvature change only on the illuminated side. The curvature change induced a change in the roller's center of mass, resulting in rolling on the surface (*37*).

Flapping butterfly-like wings

We attempted to mimic flying creatures, such as the butterfly, to demonstrate the potential of the LiLBot in generating sunlight-powered flapping motion of a pair of wings for future microscale solar aerial vehicles. To achieve the proposed potential sunlight operation, a number of challenges need to be addressed. Traditionally, the oscillator oscillates around the incident light (in an aligned configuration), which makes it difficult to initiate oscillation of horizontally oriented wings with an overhead light (in a perpendicular configuration). Moreover, the oscillation frequencies, amplitudes, and phase angles of the two wings need to be the same to enable stable flapping. Here, to overcome the above challenges, we designed and constructed two butterfly wings attached on a

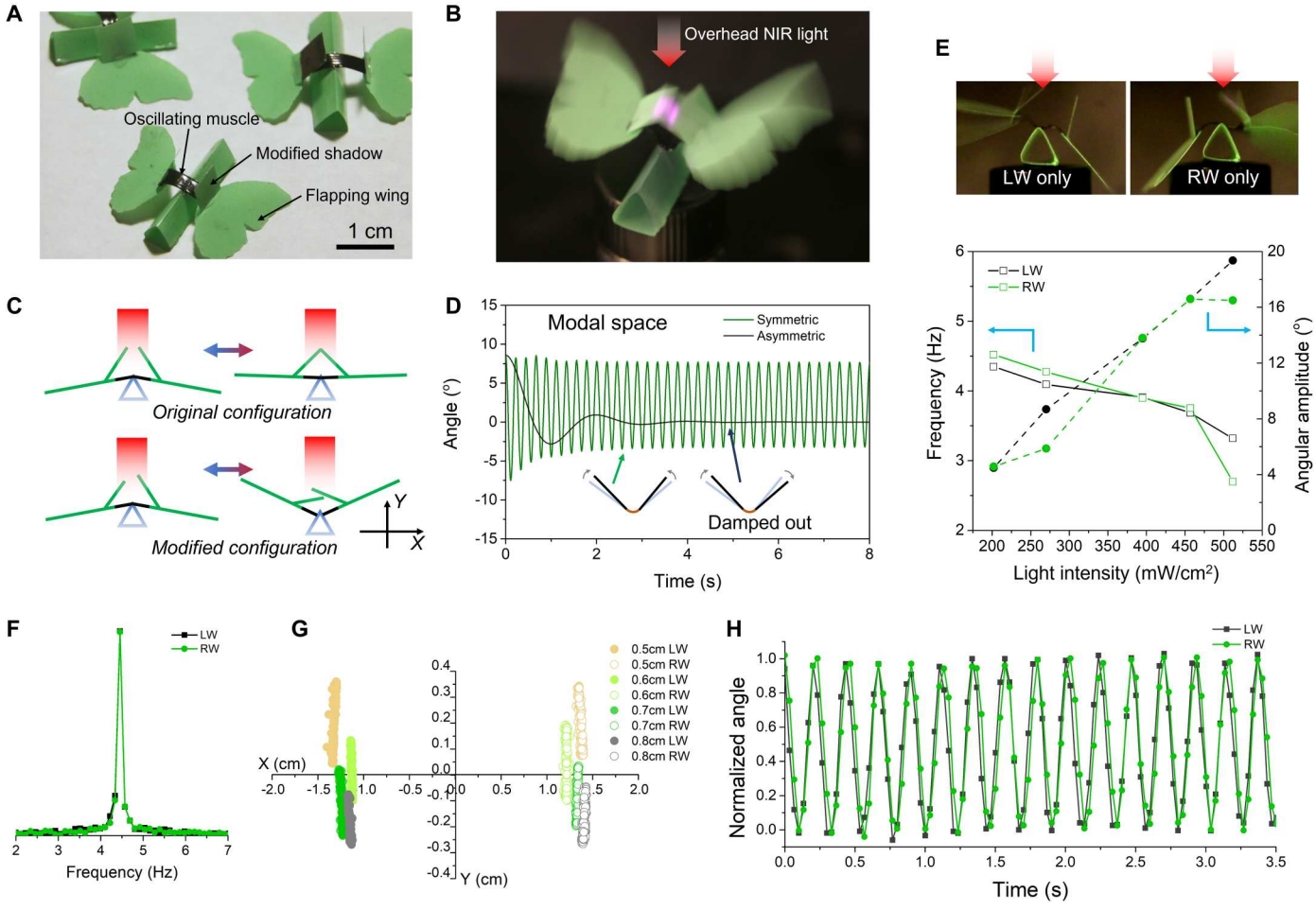

Fig. 4. Synchronized flapping butterfly-like wings. (**A**) Photograph of synthetic butterflies using PET films for the body and the wings and the LiLBot for the oscillating muscle. (**B**) Front-view actuation configuration of synchronized oscillation. (**C**) Configurations of horizontally oriented wings with symmetric or staggered shadowing strips oscillating (within the *XY* plane) under overhead light illumination. (**D**) Modal space of the butterfly wing system from simulation with the initial asymmetry between two wings being −17°. (**E**) Single-wing oscillation characterization. (**F**) Frequency, (**G**) tip trajectories within the *XY* plane, and (**H**) normalized oscillation angle and phase of two wings at the synchronization state.

single CLP film, irradiated by a sunlight-mimicking overhead light to generate synchronized oscillation.

To overcome the first challenge, a shadowing strip was attached on the wing with an angle (Fig. 4, A to C). When illuminated by an overhead light, the CLP film curled up and lifted the wing, with a tendency to track the light. However, the shadowing strip soon blocked the light before the wing could track the light. With this geometric design, the oscillation direction does not have to be aligned with light direction; the oscillation can occur perpendicular to the incident light, mimicking natural sunlight on butterfly wings.

Subsequently, we assembled two wings symmetrically on the two ends of the CLP film and attached the middle of the CLP film on a stand as the body of the butterfly (Fig. 4, A and C). A single-wing oscillation mode could be generated by applying light exclusively on one side. Variations between frequency and amplitude of the two wings due to light intensity (Fig. 4E) were observed, caused by the fabrication error and manual alignment of light for the left wing (LW) and right wing (RW). By moving the illumination spot closer to the center of the CLP film, we observed antiphase synchronized oscillation. The side exposed to more light triggered a larger amplitude than the side that harvested less light (fig. S22). The antiphase synchronization yielded the same frequency between LW and RW, regardless of the amplitude difference (fig. S20C). When we carefully adjusted the light position precisely at the center of the CLP muscle, the two wings displayed synchronized oscillations of the same frequency, amplitude, and phase angle for both wings (Fig. 4, F to H, and fig. S23). Thus, these two flapping wings interacted and coupled the motions into a dynamic steady state.

The synchronization arose from the symmetry in the geometry and mechanical properties of the wings, the inherent damping in the material, and the symmetric excitation induced by the LCE layer. Because the geometry and mechanical properties of the wings were mirrored, the motion of the system could be decoupled into two modes: the symmetric mode and the asymmetric mode. In the modal space, the symmetric excitation induced by the light shedding on the LCE layer only excited the symmetric mode (Fig. 4D and fig. S24). The photo–thermal-mechanical coupling

consistently injects mechanical energy into this mode, keeping the butterfly oscillating symmetrically with a stable amplitude. The symmetric excitation is perpendicular to and thus injects no energy into the asymmetric motion pattern in the modal space. The asymmetric motion is only subject to damping (from testbed friction and air viscosity) and restoration (from gravity) forces in the modal space. As a result, any asymmetric disturbance is damped out, leaving only the synchronized symmetric motion. On the basis of the simulation model from a single oscillator, we further established the two-wing model and successfully correlated the experimental results with simulation (discussion S3.3). With different asymmetric initial conditions (θ_1-θ_2 = 0° to 54°), and as a result of the existence of gravitational restoration force and ambient damping, the system eventually oscillated around 3° (fig. S25). Therefore, the stability of the synchronized oscillation was verified.

The synchronization of two flapping wings could be modified by geometry and intensity. We observed that decreasing the shadowing strip length gradually from 0.8 to 0.5 cm led to an elevation of oscillation position and an increase in the bending angle (Fig. 4G and fig. S26). For the 0.7-cm-length scenario, the in-phase synchronization effect could be maintained from 270 to 457 mW cm^{-2}; however, light intensity higher than 512 mW cm^{-2} led to unsteady amplitude variation over time. This was likely because of the collision and interference of two shadowing strips and resulted in 10° flapping amplitude in maximum. We bypassed the issue by placing them in staggered positions and reached a peak-to-peak amplitude up to 30° at 783 mW cm^{-2} (Fig. 4B modified configuration and figs. S27 and 28). Although promising, the current wing system did not show a lifting force by weighing mass on a balance with and without oscillation. However, future improvements to the system will be required, such as introducing nonreciprocal motion, increasing energy density of oscillation (peak-to-peak amplitude greater than 90° and frequency greater than 10 Hz), and decreasing the weight of the soft robot.

DISCUSSION

In this work, we reported a low-intensity LCE bilayer oscillator under constant nonpolarized light. The operation intensity under 1 Sun was successfully achieved, about 75% lower than the power thresholds of state-of-the-art LC materials. The mild operation window benefited from the low T_{NI} LCE while ensuring high photothermal efficiency, high responsiveness, and low storage and loss modulus. Specifically, the LCE synthesized via thiol-ene Michael addition featured low modulus (1.24 MPa), low response temperature (T_{NI} = 40°C), and large uniaxial contraction (30%). As a broad-spectrum photoabsorber, CS was well dispersed in the LCE, providing the CS-LCE composite with a high photothermal conversion efficiency. The CS-LCE thin films were three-dimensionally (3D)–printed by direct ink writing (DIW), which can enable the precise control of molecular orientation and geometry (fig. S8). To facilitate high-response out-of-plane bending, we used a CS-LCE/PDMS bilayer structure that successfully boosted the ratio of bending and recovery (bending curvature equivalent to 1.24 mm^{-1} at 70°C), critical factors of oscillation. We demonstrated that LiLBot could be used to power components of untethered, small-scale soft robots, including a walker, roller, sailboat, and synchronized flying wings, presenting promising potential for self-sustainable territorial, aerial, and water-surface robots.

Although the achievable oscillation frequency (0.3 to 11 Hz) is within the lower range of natural muscles (1 to 200 Hz) (*38*), the produced energy density (6 J m^{-3}) is still far below the theoretical energy density of LCE (55 kJ m^{-3}). This is because only partial energy storage and release of LCE were used to generate out-of-equilibrium oscillation. In addition, only the hinge (1/10 of the whole cantilever) participates in the energy conversion. Furthermore, the air damping effect is nontrivial (*12*). This can partially explain the demonstrated robots with relatively low speed, and our flapping wings can generate relatively low lifting force. Further optimization based on the working principle of oscillation in followup studies includes improvement of responsiveness in LCE material (*30*, *32*), thermal insulation, photothermal energy conversion, and structural optimization of active-passive configuration (*39*).

Although there are numerous capabilities and functions of soft robots reliant on oscillation as a self-sustainable mechanism with low energy input, there still exist many challenges when high-power density actuators are required. For instance, to meet the capabilities of flying robots, a threshold power density is required to produce meaningful thrust. We expect that those challenges could be solved with more advances in material science and engineering.

MATERIALS AND METHODS

Materials

Diacrylate LC monomers RM82 and RM257 were purchased from Shijiazhuang Sdyano Fine Chemical Co. Ltd. 2,2-(Ethylenedioxy)-diethanethiol (EDDET), 1,3,5-triallyl-1,3,5-triazine-2,4,6(1H,3H,5H)-trione (TATATO), I-369, butylated hydroxytoluene (BHT), and 3-(trimethoxy silyl)propyl methacrylate (TMSPMA) were purchased from Sigma-Aldrich. PDMS kits were Silgard 184. All chemicals were used as received without further purification.

Material fabrication

CS was deposited by placing aluminum foil above the flame and washed with hexane. PDMS film (curer:base = 1:5) was spin-coated on clean glass slides with certain rotating speed and cured on an 80°C hot plate. Silane-containing double bonds were grown by vapor phase deposition of TMSPMA after oxygen plasma of PDMS. LCE was fabricated by the previously reported thiol-ene click reaction (*32*). Specifically, 0.857 g of RM82 and 0.25 g of RM257 were preheated to melt, and then 0.387 g of EDDET, 0.056 g of TATATO, 0.024 g of BHT, 0.03 g of I-369, and 0.008 g of CS were added to the solution and mixed for 10 min. The CS was dispersed via probe sonication for 1.5 min. Then, 25 μl of triethanolamine (TEA) were added to the solution, followed by thorough mixing. The ink was cured in a syringe at 65°C for 3 hours to form an oligomerized ink. We used a DIW printer (CELLINK, BIO X) to print LCE directly on PDMS. The printing speed was 7 mm s^{-1}, and the pneumatic pressure was 700 kPa. After printing, the sample was UV-polymerized for 5 min on two sides to fix the orientation. The CS-LCE/PDMS film was peeled with a razor blade and used as a single oscillating cantilever or as a hinge material. For butterfly wings, we used a laser cutter to obtain identical wing shapes.

Characterization

The nematic-to-isotropic transition temperature of LCE ink was measured by differential scanning calorimetry (DSC-Q8000) under a second heating cycle (−30° to 100°C at a ramp rate of 10 °C min^{-1}). Storage modulus and loss modulus were measured using a dynamic mechanical analyzer (TA Instruments, DMA850) at a heating rate of 5°C min^{-1}, a sweep frequency of 1 Hz, and a temperature range from room temperature to 95°C. The actuation ratio was recorded by an Apple iPhone X and analyzed using ImageJ. Absorbance spectra were characterized by UV-vis-NIR spectroscopy (Shimazu, UV-3101PC). Temperature changes upon NIR laser were measured by a thermocouple placed on the surface of a CLP film. Cross-sectional images of the CLP film were taken by a ZEISS Supra 40VP SEM. Linear contraction and bending under heat were accomplished on a hot plate. Light-driven oscillation was achieved by hanging samples on a 3D-printed holder and applying light horizontally. NIR light was provided by an infrared laser pointer (SKY; 808 nm, 1500 mW). The intensity of the NIR light was controlled by a dc power supply and calibrated via a silicon-based standard photodiode sensor (Thorlabs, PM16-121) with a reflective ND filter (Thorlabs, ND10A). Movies of oscillation were recorded with a smartphone and a digital camera. All trajectories were analyzed using the software Tracker (version 5.0.5). For calculating the frequency of the synchronized butterfly flapping demonstrations, we used Excel to carry out a fast Fourier transform analysis.

Supplementary Materials

This PDF file includes:
Supplementary Methods
Supplementary Discussion
Figs. S1 to S28
Tables S1 and S2
References (*40*–*45*)

Other Supplementary Material for this manuscript includes the following:
Movies S1 to S7

REFERENCES AND NOTES

1. P. Rothemund, Y. Kim, R. H. Heisser, X. Zhao, R. F. Shepherd, C. Keplinger, Shaping the future of robotics through materials innovation. *Nat. Mater.* **20**, 1582–1587 (2021).
2. C. Laschi, B. Mazzolai, M. Cianchetti, Soft robotics: Technologies and systems pushing the boundaries of robot abilities. *Sci. Robot.* **1**, eaah3690 (2016).
3. S. I. Rich, R. J. Wood, C. Majidi, Untethered soft robotics. *Nat. Electron.* **1**, 102–112 (2018).
4. A. H. Gelebart, D. Jan Mulder, M. Varga, A. Konya, G. Vantomme, E. W. Meijer, R. L. B. Selinger, D. J. Broer, Making waves in a photoactive polymer film. *Nature* **546**, 632–636 (2017).
5. Y. Zhai, T. N. Ng, Self-sustained robots based on functionally graded elastomeric actuators carrying up to 22 times their body weight. *Adv. Intell. Syst.* **2100085**, 2100085 (2021).
6. K. Kruse, F. Jülicher, Oscillations in cell biology. *Curr. Opin. Cell Biol.* **17**, 20–26 (2005).
7. A. Vilfan, T. Duke, Synchronization of active mechanical oscillators by an inertial load. *Phys. Rev. Lett.* **91**, 114101 (2003).
8. R. K. Josephson, J. G. Malamud, D. R. Stokes, Review asynchronous muscle: A primer. *J. Exp. Biol.* **203**, 2713–2722 (2000).
9. R. Yoshida, T. Ueki, Evolution of self-oscillating polymer gels as autonomous polymer systems. *NPG Asia Mater.* **6**, e107–e107 (2014).
10. P. Rothemund, A. Ainla, L. Belding, D. J. Preston, S. Kurihara, Z. Suo, G. M. Whitesides, A soft, bistable valve for autonomous control of soft actuators. *Sci. Robot.* **3**, eaar7986 (2018).
11. X. Q. Wang, C. F. Tan, K. H. Chan, X. Lu, L. Zhu, S. W. Kim, G. W. Ho, In-built thermo-mechanical cooperative feedback mechanism for self-propelled multimodal locomotion and electricity generation. *Nat. Commun.* **9**, 3438 (2018).
12. S. Serak, N. Tabiryan, R. Vergara, T. J. White, R. A. Vaia, T. J. Bunning, Liquid crystalline polymer cantilever oscillators fueled by light. *Soft Matter* **6**, 779–783 (2010).
13. Y. Zhao, C. Xuan, X. Qian, Y. Alsaid, M. Hua, L. Jin, X. He, Soft phototactic swimmer based on self-sustained hydrogel oscillator. *Sci. Robot.* **4**, eaax7112 (2019).
14. H. Zeng, M. Lahikainen, L. Liu, Z. Ahmed, O. M. Wani, M. Wang, A. Priimagi, Light-fuelled freestyle self-oscillators. *Nat. Commun.* **10**, 5057 (2019).
15. K. M. Lee, M. L. Smith, H. Koerner, N. Tabiryan, R. A. Vaia, T. J. Bunning, T. J. White, Photodriven, flexural-torsional oscillation of glassy azobenzene liquid crystal polymer networks. *Adv. Funct. Mater.* **21**, 2913–2918 (2011).
16. X. Qian, Y. Zhao, Y. Alsaid, X. Wang, M. Hua, T. Galy, H. Gopalakrishna, Y. Yang, J. Cui, N. Liu, M. Marszewski, L. Pilon, H. Jiang, X. He, Artificial phototropism for omnidirectional tracking and harvesting of light. *Nat. Nanotechnol.* **14**, 1048–1055 (2019).
17. T. J. White, N. V. Tabiryan, S. V. Serak, U. A. Hrozhyk, V. P. Tondiglia, H. Koerner, R. A. Vaia, T. J. Bunning, A high frequency photodriven polymer oscillator. *Soft Matter* **4**, 1796–1798 (2008).
18. L. Yang, L. Chang, Y. Hu, M. Huang, Q. Ji, P. Lu, J. Liu, W. Chen, Y. Wu, An autonomous soft actuator with light-driven self-sustained wavelike oscillation for phototactic self-locomotion and power generation. *Adv. Funct. Mater.* **30**, 1908842 (2020).
19. A. H. Gelebart, G. Vantomme, E. W. Meijer, D. J. Broer, Mastering the photothermal effect in liquid crystal networks: A general approach for self-sustained mechanical oscillators. *Adv. Mater.* **29**, 1606712 (2017).
20. X. Dong, J. Xu, X. Xu, S. Dai, X. Zhou, G. Cheng, N. Yuan, J. Ding, Sunlight-driven continuous flapping-wing motion. *ACS Appl. Mater. Interfaces* **12**, 6460–6470 (2020).
21. R. Lan, J. Sun, C. Shen, R. Huang, Z. Zhang, L. Zhang, L. Wang, H. Yang, Near-infrared photodriven self-sustained oscillation of liquid-crystalline network film with predesignated polydopamine coating. *Adv. Mater.* **32**, e1906319 (2020).
22. Y. Chen, J. Yang, X. Zhang, Y. Feng, H. Zeng, L. Wang, W. Feng, Light-driven bimorph soft actuators: Design, fabrication, and properties. *Mater. Horiz.* **8**, 728–757 (2021).
23. G. Vantomme, L. C. M. Elands, A. H. Gelebart, E. W. Meijer, A. Y. Pogromsky, H. Nijmeijer, D. J. Broer, Coupled liquid crystalline oscillators in Huygens' synchrony. *Nat. Mater.* **20**, 1702–1706 (2021).
24. X. Yue, Z. Zhang, T. Zhang, D. Yang, J. Xu, F. Qiu, Simply realizing durable PVDF/candle soot foam with excellent solar absorption for solar-assisted recovery of heavy oil spill. *J. Taiwan Inst. Chem. Eng.* **128**, 187–193 (2021).
25. S. Wu, Y. Du, Y. Alsaid, D. Wu, M. Hua, Y. Yan, B. Yao, Y. Ma, X. Zhu, X. He, Superhydrophobic photothermal icephobic surfaces based on candle soot. *Proc. Natl. Acad. Sci. U.S.A.* **117**, 11240–11246 (2020).
26. P. Shi, Y. Zhao, Z. Liu, X. He, Liquid crystal elastomer composite-based photo-oscillator for microrobots. *J. Compos. Mater.* **57**, 633–644 (2023).
27. L. Dong, X. Tong, H. Zhang, M. Chen, Y. Zhao, Near-infrared light-driven locomotion of a liquid crystal polymer trilayer actuator. *Mater. Chem. Front.* **2**, 1383–1388 (2018).
28. Y. Xiao, J. Lin, J. Xiao, M. Weng, W. Zhang, P. Zhou, Z. Luo, L. Chen, A multi-functional light-driven actuator with an integrated temperature-sensing function based on a carbon nanotube composite. *Nanoscale* **13**, 6259–6265 (2021).
29. R. Tang, W. Sang, Y. Wu, C. Zhu, J. Liu, Multi-wavelength light drivable oscillatory actuator on graphene-based bilayer film. *Macromol. Mater. Eng.* **302**, 1600384 (2017).
30. M. O. Saed, R. H. Volpe, N. A. Traugutt, R. Visvanathan, N. A. Clark, C. M. Yakacki, High strain actuation liquid crystal elastomers via modulation of mesophase structure. *Soft Matter* **13**, 7537–7547 (2017).
31. M. O. Saed, A. H. Torbati, C. A. Starr, R. Visvanathan, N. A. Clark, C. M. Yakacki, Thiol-acrylate main-chain liquid-crystalline elastomers with tunable thermomechanical properties and actuation strain. *J Polym Sci B* **55**, 157–168 (2017).
32. M. O. Saed, C. P. Ambulo, H. Kim, R. De, V. Raval, K. Searles, D. A. Siddiqui, J. M. O. Cue, M. C. Stefan, M. R. Shankar, T. H. Ware, Molecularly-engineered, 4D-printed liquid crystal elastomer actuators. *Adv. Funct. Mater.* **29**, 1806412 (2019).
33. S. Li, H. Bai, Z. Liu, X. Zhang, C. Huang, L. W. Wiesner, M. Silberstein, R. F. Shepherd, Digital light processing of liquid crystal elastomers for self-sensing artificial muscles. *Sci. Adv.* **7**, eabg3677 (2021).
34. K. Kumar, C. Knie, D. Bléger, M. A. Peletier, H. Friedrich, S. Hecht, D. J. Broer, M. G. Debije, A. P. H. J. Schenning, A chaotic self-oscillating sunlight-driven polymer actuator. *Nat. Commun.* **7**, 11975 (2016).
35. T. Qiu, T. C. Lee, A. G. Mark, K. I. Morozov, R. Münster, O. Mierka, S. Turek, A. M. Leshansky, P. Fischer, Swimming by reciprocal motion at low Reynolds number. *Nat. Commun.* **5**, 5119 (2014).
36. M. Rogóż, H. Zeng, C. Xuan, D. S. Wiersma, P. Wasylczyk, Light-driven soft robot mimics caterpillar locomotion in natural scale. *Adv. Opt. Mater.* **4**, 1689–1694 (2016).
37. X. Lu, S. Guo, X. Tong, H. Xia, Y. Zhao, Tunable photocontrolled motions using stored strain energy in malleable azobenzene liquid crystalline polymer actuators. *Adv. Mater.* **29**, 1606467 (2017).

38. M. Duduta, E. Hajiesmaili, H. Zhao, R. J. Wood, D. R. Clarke, Realizing the potential of dielectric elastomer artificial muscles. *Proc. Natl. Acad. Sci. U.S.A.* **116**, 2476–2481 (2019).
39. Y. Kim, J. van den Berg, A. J. Crosby, Autonomous snapping and jumping polymer gels. *Nat. Mater.* **20**, 1695–1701 (2021).
40. G. Vantomme, A. H. Gelebart, D. J. Broer, E. W. Meijer, A four-blade light-driven plastic mill based on hydrazone liquid-crystal networks. *Tetrahedron* **73**, 4963–4967 (2017).
41. G. Vantomme, A. H. Gelebart, D. J. Broer, E. W. Meijer, Self-sustained actuation from heat dissipation in liquid crystal polymer networks. *Polym. Chem.* **56**, 1331–1336 (2018).
42. W. Wei, Z. Zhang, J. Wei, X. Li, J. Guo, Phototriggered selective actuation and self-oscillating in dual-phase liquid crystal photonic actuators. *Adv. Opt. Mater.* **6**, 1800131 (2018).
43. Y. Li, Y. Liu, D. Luo, Polarization dependent light-driven liquid crystal elastomer actuators based on photothermal effect. *Adv. Opt. Mater.* **9**, 2001861 (2021).
44. M. Lahikainen, H. Zeng, A. Priimagi, Design principles for non-reciprocal photomechanical actuation. *Soft Matter* **16**, 5951–5958 (2020).
45. Z. Hu, Y. Li, J.-a. Lv, Phototunable self-oscillating system driven by a self-winding fiber actuator. *Nat. Commun.* **12**, 3211 (2021).

Acknowledgments

Funding: The research was supported by NSF CAREER award 1724526; AFOSR awards FA9550-17-1-0311, FA9550-18-1-0449, and FA9550-20-1-0344; and ONR awards N000141712117 and N00014-18-1-2314. **Author contributions:** X.H. conceived the concept, planned the project, and supervised the research. Y.Z. designed and conducted the experiments and data analysis. Y.Z. and P.S. conducted the fabrication and characterization. Q.L. and Z.L. developed the simulation and theory under supervision of M.K.J. All authors wrote the manuscript. All authors have given approval to the final version of the manuscript. **Competing interests:** The authors declare that they have no competing interests. **Data and materials availability:** All data needed to evaluate and support the conclusions in the manuscript are included in the main text or the Supplementary Materials. Contact Y.Z. for any questions. All data including modeling data have been deposited on Zenodo: https://zenodo.org/record/7754792. Correspondence and requests for materials should be addressed to X.H. (e-mail: ximinhe@ucla.edu).

Submitted 24 November 2022
Accepted 22 March 2023
Published 19 April 2023
10.1126/scirobotics.adf4753

Science Robotics

Sunlight-powered self-excited oscillators for sustainable autonomous soft robotics

Yusen Zhao, Qiaofeng Li, Zixiao Liu, Yousif Alsaid, Pengju Shi, Mohammad Khalid Jawed, and Ximin He

Sci. Robot., **8** (77), eadf4753.
DOI: 10.1126/scirobotics.adf4753

Science Robotics (ISSN) is published by the American Association for the Advancement of Science. 1200 New York Avenue NW, Washington, DC 20005. The title *Science Robotics* is a registered trademark of AAAS.